Available online at www.sciencedirect.com

jmr&t Journal of Materials Research and Technology

journal homepage: www.elsevier.com/locate/jmrt

Original Article

Analysis of structural and chemical inhomogeneity of thin films developed on ferrite grains by color etching with Beraha-I type etchant with spectroscopic ellipsometry and XPS

József Bálint Renkó [a], *Alekszej Romanenko* [b,c], *Péter János Szabó* [a], *Attila Sulyok* [b], *Péter Petrik* [b], *Attila Bonyár* [d,*]

[a] *Department of Materials Science and Engineering, Faculty of Mechanical Engineering Budapest University of Technology and Economics, Budapest, Hungary*
[b] *Centre for Energy Research, Institute of Technical Physics and Materials Science (MFA), Budapest, Hungary*
[c] *Doctoral School of Chemistry, Eötvös Loránd University, Budapest, Hungary*
[d] *Department of Electronics Technology, Faculty of Electrical Engineering and Informatics, Budapest University of Technology and Economics, Budapest, Hungary*

ARTICLE INFO

Article history:
Received 11 February 2022
Accepted 25 March 2022
Available online 31 March 2022

Keywords:
Color etching
Spectroscopic ellipsometry
Grain orientation
Low carbon steel
X-ray photoelectron spectroscopy

ABSTRACT

The structural and chemical homogeneity of the developed thin film upon color etching a low-carbon steel specimen with Beraha-I type color etchant was investigated by spectroscopic ellipsometry and electron backscatter diffraction examinations. The obtained layer thickness maps showed a good correlation with the crystallographic orientation of the individual ferrite grains, corresponding well with previous studies that found a relation between etching and layer build-up speeds and the <100>, <111> directions. However, the refractive index map also showed a dependence on the grain orientation, which contradicts previous models that treat the developed interfering layer as a homogenous material with a constant refractive index and chemical composition. Scanning ellipsometry and X-ray photoelectron spectroscopy measurements confirmed that the chemical composition and refractive index of the developed layer are inhomogeneous both along the surface and the thickness of the film. It was shown that the developed layer consists of mainly oxides and sulfides and that the oxygen content decreases, while the Fe content increases along the normal direction from the surface of the film, in good agreement with the increasing refractive index. The observed differences can be related to the different etching speeds of the ferrite grains (Fe dissolution rate), depending on their orientation.
© 2022 The Author(s). Published by Elsevier B.V. This is an open access article under the CC BY-NC-ND license (http://creativecommons.org/licenses/by-nc-nd/4.0/).

* Corresponding author.
E-mail address: bonyar@ett.bme.hu (A. Bonyár).
https://doi.org/10.1016/j.jmrt.2022.03.159
2238-7854/© 2022 The Author(s). Published by Elsevier B.V. This is an open access article under the CC BY-NC-ND license (http://creativecommons.org/licenses/by-nc-nd/4.0/).

1. Introduction

Various etching methods used widely in metallography offer a quick and easy solution for developing the grain structure of different samples [1–3]. The etchant reacts with the surface of the sample to change its topography, thus making the individual grains and grain boundaries visible [4–7]. Although there are not many differences in their field of application, they can be divided into multiple groups according to their working principle [8].

Color etchants belong to one of these groups [9,10]. Although these are also widely used methods, they are less common than chemical etchants [11], mainly because the saline solutions used in color etching are less aggressive [12]. Thus, fewer types are available, and it takes significantly longer to achieve the proper effect than chemical etchants [13–15]. While chemical etchants need only a few seconds, color etching methods need at least a few minutes to develop an adequately thick, transparent surface layer [16]. The layer grows in both directions relative to the original plane of the sample surface as more and more material dissolves from the sample and the etchant [17]. As the film grows, each particle undergoes a cyclic color change [18].

Although these various color etching processes have been widely used, the chemical processes involved in etching are not or only partially being explored. Understanding the etching phenomenon represents a relatively new direction in materials science, most of which can be traced back to the past decade. Research groups have made efforts to understand the correlation revealed between the specificity of the layer formed during color etching and the crystallographic grain orientation [19]. The relationship between the color and orientation was first shown in 2007 by Kardos et al., who compared the color and intensity of the individual particles after etching and the angle enclosed by the <100> crystallographic direction determined by electron backscatter diffraction (EBSD) analysis [20]. In 2012, it was proven that the thickness of the film formed during color etching varies depending on the orientation of the grain, and it also increases in both directions compared to the original surface of the sample [21]. Britz and his colleagues tried to understand the process from a different direction. A unique incubator system was built, and by further developing the equipment in several steps, they were able to keep the etching process under well-controlled conditions [22,23]. Using the incubator, well-reproducible etchings could be performed with LePera reagent on low-carbon steel samples. The reproducibility problem was solved; however, the etching processes have still not been explored [24]. Others targeted the chemical composition and structure of the formed layer. Bioud et al., in 2016 examined the structure and chemical composition of GaAs-based thin films created by chemical and electrochemical etching [25].

In 2019, in a comprehensive study, our group devised a method to properly relate the color of the interfering layer to specific crystallographic grain orientations [17]. In our proposed model, we presumed that the thickness of the developed layer (d) depends on several factors, as in Eq. (1):

$$d = \int_0^{t_e} v(t, h_o, \theta, T, v_f, C, c,)\, dt \quad (1)$$

The first and most crucial factor is etching time (t), The chemical reaction between the etchant and the bulk of the sample can be delayed if an oxide layer (h_o) covers the surface. After the etching of the metal began, the etching speed (v) depends heavily on the crystallographic orientation of the individual grains (θ). Other factors, such as the temperature and etchant flow rate ($v|f$) can also affect the thickness of the resulting layer. Last but not least, it is also essential to mention material composition (C) and etchant concentration (c) as factors, although they are not supposed to be changed during etching.

This model made it possible to determine the average etching rates and layer development speeds for each individual grain and thus assign the developed colors after fixed etching times to characteristic crystallographic orientations. As a result, a method was developed that enabled the angle determination between the surface normal and the <100>, <111> directions for individual ferrite grains, with an average absolute error of only 3°, by using solely optical microscopy [17].

The current work aims to verify and further refine the previously established model, and thus increase the accuracy of the proposed method. For the sake of simplicity, our model presumed that the chemical composition and thus refractive index (RI) is homogeneous for the developed interference layer. Since the observed color greatly depends on the RI of the layer, any perturbation would cause a significant variance that decreases the accuracy of orientation estimation based on the developed color. Thus, our aim here is to investigate the homogeneity of the chemical composition of the developed layer. For this purpose, spectroscopic ellipsometry (SE) and X-ray photoelectron spectroscopy (XPS) are used.

2. Experimental

2.1. Materials and methods

With SE, the refractive index and thickness of nanometer-sized layers can be measured [26]. However, the diameter of the smallest area that can be scanned with it is approx. 0.3 mm, so it was necessary to use a material in which the grains could be enlarged above this size, thus allowing direct thickness measurement of the individual grains. In our previous experiments, spheroidal graphite cast iron was etched with fresh Beraha I solution, which is obtained by dissolving 3 g $K_2S_2O_5$ and 10 g $Na_2S_2O_3$ in 100 ml distilled water. Unfortunately, it was not possible to increase the grain size of the cast iron sample to the desired range. In order to be able to continue our tests without changing the etchant, we have chosen DC01 low carbon steel as the experimental material. DC01 contains only a ferritic phase, which can easily react with the Beraha I etchant. The chemical composition of the selected ferritic material as measured by spark optical emission spectroscopy is shown in Table 1.

Table 1 – Chemical composition of DC01 ferritic steel [atomic%].

Fe	C	Mn	Cr	Mo	Ni	Al	Co	Cu	Nb
98.9	0.092	0.616	0.081	0.013	0.034	0.064	0.017	0.118	0.065

To achieve the required grain size, the sample was heated up to 850 °C and then annealed, thus providing the slow cooling required for maximum effect. Further experiment steps were performed in air-conditioned laboratories, in which the temperature was set to 21 °C.

Color etching of the polished sample took 60 s. It was then rinsed in distilled water for 45 s to stop the etching process. To aid in de-watering and faster drying of the layer, it was immersed in alcohol for 15 s. Finally, the surface was dried with compressed air. A flowchart of the used sample preparation and experimental procedures is presented in Fig. 1.

2.2. Spectroscopic ellipsometry

The main optical method used to characterize the developed thin films is SE. It illuminates the surface of the sample with light of known polarization and measures the changes in polarization that occurs during reflection [27]. Ellipsometry can determine the phase difference between the two polarization directions, which makes it much more sensitive than conventional reflectometry. Accuracy of up to 1 Å can be achieved in the layer thickness measurement. In addition, the refractive index (RI) can also be determined with an accuracy of 0.001 [28]. The measurement over a wide spectral range allows the modeling of complex layer structures and the determination of their parameters. Since it can be performed not more than a few seconds, it is also possible to map larger surfaces in a realistic time [29].

The resin-embedded sample was placed on a workbench of a Woollam M–2000 DI rotating compensator spectroscopic ellipsometer with a wavelength range between 190 nm and 1690 nm. To prevent unintentional position alteration of the sample during mapping, the sample was fixed to the worktable before each mapping. The measurements at each point lasted a total of 2 × 16 s, the step size was 175 μm, and the mapped surface was 1.4 × 1.4 cm^2. Due to the large angle of incidence (~70°), the spot was elongated in the direction of the plane of incidence according to the trigonometry.

Since SE is a highly surface-sensitive method, proper consideration of the surface is paramount when determining the bulk RI of materials. Unfortunately, in our case, we cannot assume that the refractive index of the substrate is constant, and only the thickness of the surface layer is different. Grains oriented in different directions have different optical properties. Thus, we created an optical model in which the dispersions of the surface layer and the steel substrate at each measurement point were described by a Cauchy (polynomial) dispersion and Lorentz oscillators, respectively [30].

Two similar approaches were used to characterize the depth dependence of the refractive index of the surface layer. In both methods, the applied polynomial Cauchy dispersion formula was the same as in Eq. (2), and the only difference occurred in parameter A.

$$RI = A + \frac{B}{\lambda^2} + \frac{C}{\lambda^4} \quad (2)$$

In the first approach, A was a constant, thus determining the RI for the whole layer. In the second one, A was described by an exponential function resulting in a monotonous decrease in the RI along the thickness of the etched layer as moving away from the surface of the substrate (Fig. 2).

Due to the nature of Cauchy dispersion, the used parameter A is a good approximation of the RI. In the case of the exponentially decaying Cauchy dispersion, the RI of the layer would change along the thickness, and the two fitting methods would not be comparable. Thus, to be able to compare the different fitting methods, parameter A was used instead of the RI. Due to the changes of A along the thickness in the second case, the evaluation of exponential fitting was done for the maximal value of A, which is at the ferrite–layer interface.

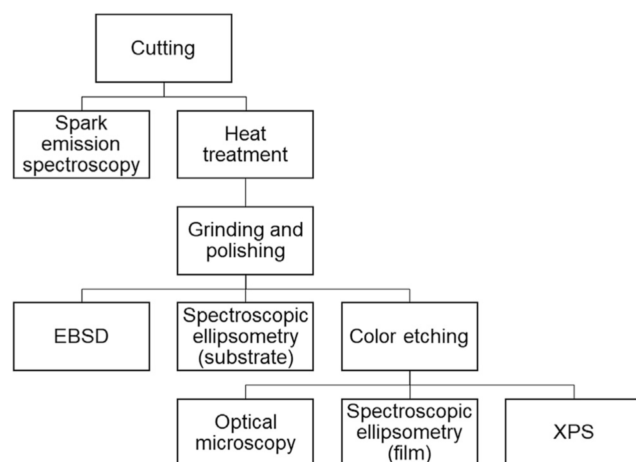

Fig. 1 – Flowchart of the sample handling and experimental procedures.

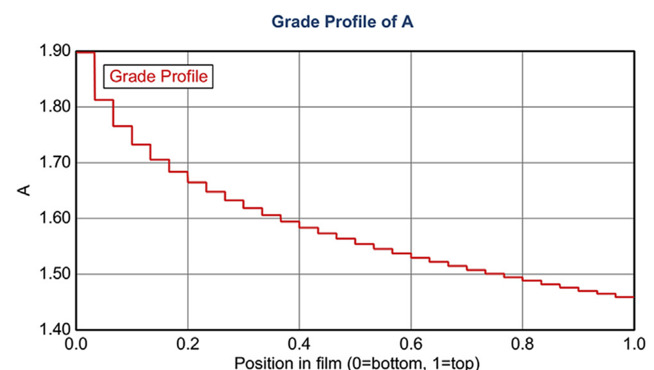

Fig. 2 – Change of parameter A in the applied exponential Cauchy dispersion.

2.3. XPS

X-ray photoelectron spectroscopy (XPS) analysis were carried out under ultrahigh vacuum conditions ($2*10^{-9}$ mbar). The samples were mounted to a sample holder by using a sticking carbon tape. The specimens were exposed to 70 °C heat treatment for 48 h, which is the standard baking procedure of the applied vacuum system. The photoelectron spectra were obtained by using X-ray radiation from an Al anode with 15 keV excitation. Constant energy resolution of 1.5 eV was provided by a special cylindrical mirror analyzer with retarding field (type DESA 150, Staib Instruments Ltd.). All spectra were recorded with 0.1 eV energy steps.

The binding energy of observed XPS peaks was determined by using the 284.6 eV value of adventitious carbon as a reference peak. The following peaks were measured and listed with binding energies in Table 2.

The observed XPS peaks yield information for the average composition of a limited volume at the surface region of the specimen. The detected spot is determined by the analyzer's focus area, which is around 5 mm in diameter. The information depth is determined by the inelastic mean free paths of photoelectrons, ranging between 1.4 nm (in case of Fe) to 2 nm (in case of S).

The state of the surface showed some organic contamination that is usual on surfaces arriving from open air. In order to reveal the accurate composition of the layer, ion sputtering was applied. A further dose of ion sputtering was applied to reach and reveal an increased layer depth. Ion sputtering conditions: 1 keV Ar + beam scanned over the surface to assure an even sputtering of the whole observed area; 75° angle of incidence. The vacuum pressure during ion sputtering was 2.5E-7 mbar.

Elemental compositions were determined assuming a homogeneous distribution of the elements within the detected depth. After applying the usual Shirley-background subtraction, peak intensities were derived by Gaussian–Lorentzian fitting for the peak shapes. Elemental concentrations were calculated from peak areas, and sensitivity factors were taken from the literature [31].

2.4. Other instrumentation

The chemical composition of the examined low carbon steel was measured on a PMI-Master Sort optical emission spectrometer. Images of color etching were recorded with a DP72 digital camera connected to an Olympus BX51 optical microscope.

Electron backscatter diffraction was performed with a TSL-EDAX EBSD system connected to a Philips XL-30 scanning electron microscope. Since the available image size with the lowest resolution of the device is approximately 1500 × 1500 μm, dozens of shots were needed to scan the whole surface. The inverse pole figure maps of the examined surface are shown in Fig. 3c. The slight distortion seen in the pole figures is due to the tilted image capture method at a tilt angle of 70° and the uncertainties in the correction software.

3. Results and discussion

3.1. Color etching and spectroscopic ellipsometry

Figure 3a presents an optical microscopy image of the specimen after color etching. A total of 35 grains were selected on the examined surface, all of which were identifiable on the ellipsometry (Fig. 3b) and EBSD maps (Fig. 3c) as well. As can be seen in Fig. 3b, a thin film of around a hundred nanometers has been formed above the ferrite grains, and the layer thickness varies above the individual grains, making them easily identifiable on the ellipsometry layer thickness map. The calculated etching speeds can be assigned to the orientation with the EBSD images. As discussed in our previous paper, the etching speed and thin film thickness have a positive correlation with the angle between the surface normal and the <111> direction, while they have a negative correlation with the <100> direction [17].

By assuming a homogeneous material (chemical) composition for the developed layer, and a constant refractive index for the film, our introduced model enabled the determination of the orientation of ferrite grains by using optical microscopy only, with an average absolute error of 3–5°, compared to the EBSD control measurements [17].

To test this hypothesis, first, a Cauchy dispersion with a constant parameter *A* was used to obtain the refractive index and thickness parameters of the developed film from the ellipsometry measurements. The maps presented in Figs. 3 and 4 were obtained with this model (see Section 2.2. For details). In Fig. 4 the refractive index (RI), the thickness of the layer (*d*), and the mean square error of the fitted model (MSE) are shown. Thanks to the large average grain size, even with the 175 μm step size of scanning ellipsometry the individual grains are well distinguishable. For smaller grains and for grain boundaries an average of the adjacent particles were detected, and the resulting values are obtained accordingly.

The most notable information in Fig. 4 is that besides the thickness of the layer (Fig. 4b), the obtained refractive index of the layer also varies above the individual ferrite grains (Fig. 4a). The former was expected (as discussed before), however, a varying refractive index contradicts the previously proposed models that were used to calculate layer development and etching speeds. The other notable feature is that the error of model fitting on the measured psi-delta data visibly

Table 2 – Binding energy of observed XPS peaks for different elements.

Element and electron shell	Fe 2p 1/2	Fe 2p 3/2	N 1s	O 1s	C 1s	S 2p
Binding energy	720 eV	707 eV	399 eV	532 eV	285 eV	164 eV

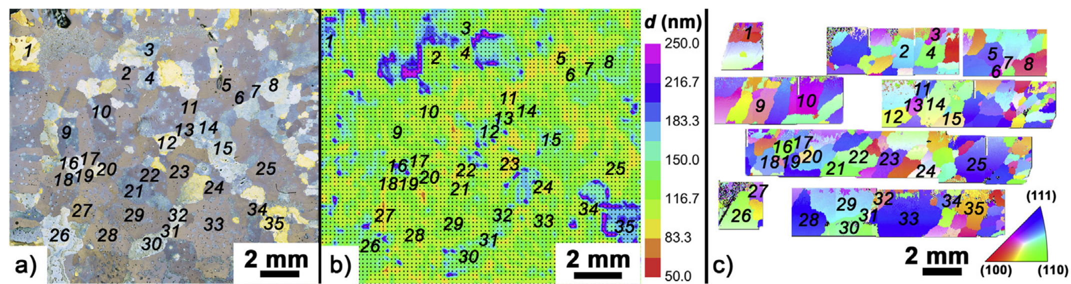

Fig. 3 – a) Optical microscope image of the color etched ferritic steel specimen (60 s in Beraha-I) with the label of the grains selected for further investigation. b) The layer thickness map (*d*) is determined by SE (with a constant Cauchy dispersion A parameter). c) The inverse pole figures of the same area from electron backscatter diffraction (EBSD).

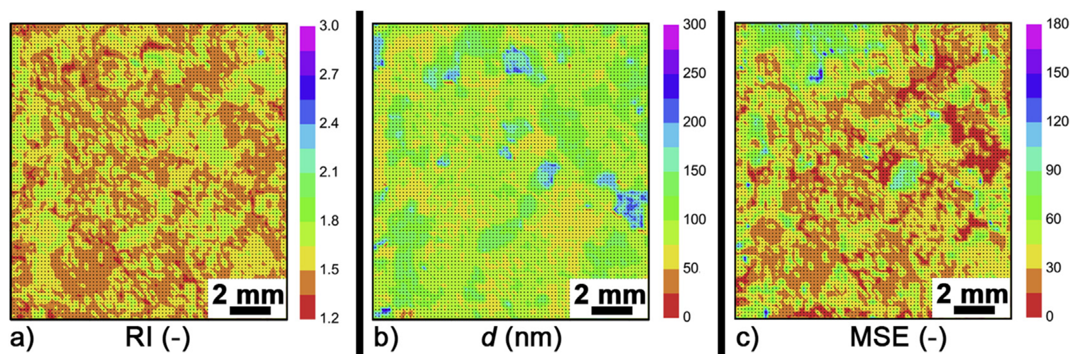

Fig. 4 – Mapping of the etched surface to show the variation of the layer's RI calculated directly next to the substrate (a), layer thickness (b), and the mean square error (MSE) maps (c) of the color etched ferritic steel specimen (60 s in Beraha-I), obtained by SE. The model applied here assumed a constant RI (Cauchy dispersion A parameter) along the thickness. The MSE represents the error of model fitting on the measured psi-delta curves at every point.

correlates with the obtained refractive index (Fig. 4c). This indicates that the used Cauchy dispersion that handles the *A* parameter as constant (in the function of the depth within the layer) does not fit well on a large set of the grains.

To investigate this further, a modified Cauchy dispersion model was fitted on the measured ellipsometry data, that handles the parameter *A* as an exponential function, that decays from the bottom of the layer (from the ferrite–layer interface) along the thickness of the layer. As can be seen on the comparison of the main square error using a constant (Fig. 5a) and an exponential decaying (Fig. 5b) *A* parameter, the modification generally decreased the error of model fitting along the whole surface. The refractive index seems to be the highest at the metal-layer interface and decays in the direction of the surface.

To quantify the ellipsometry results and compare them with the crystallographic orientation of the ferrite grains, the correlation between the angle enclosed by the three crystallographic main directions and the obtained layer thickness and the refractive index were calculated and presented in Fig. 6. The examined main crystallographic orientations were marked with their Miller indexes ([100], [110], and [111]). The angle enclosed with [110] shows almost no correlation with any investigated parameters, consistently with previous investigations [17]. Such is the negative correlation with [100] and the positive correlation with [111] in terms of layer thickness (and thus etching speed) [17].

The new information is that the RI, which was considered homogenous in the previous model, also correlates with the [100] and [111] directions, the same way as the layer thickness/etching speed does. This is true for both fitted models (constant and exponentially decaying *A* parameters). The main difference between the two fitted models is that the error of fitting (MSE) has a strong positive correlation with the parameter *A* (0.87) for the constant *A* parameter case, which indicates a big effect of the model on the obtained refractive index. This correlation drops to nearly zero for the exponentially decaying model. At the same time, the correlation between parameter *A* and the two main directions, [100] and [111] drops to a week 0.38, while it does not change significantly for the thickness. (The positive correlation between *d* and MSE can be considered normal for ellipsometry.)

All these results indicate that the orientation of the grains primarily determine the etching speed and the thickness of the developed layer. Since the refractive index is not constant along the thickness of the layer, and it decays from the ferrite–layer interface, the different layer development rates affect the depth dependent RI function of the layer indirectly.

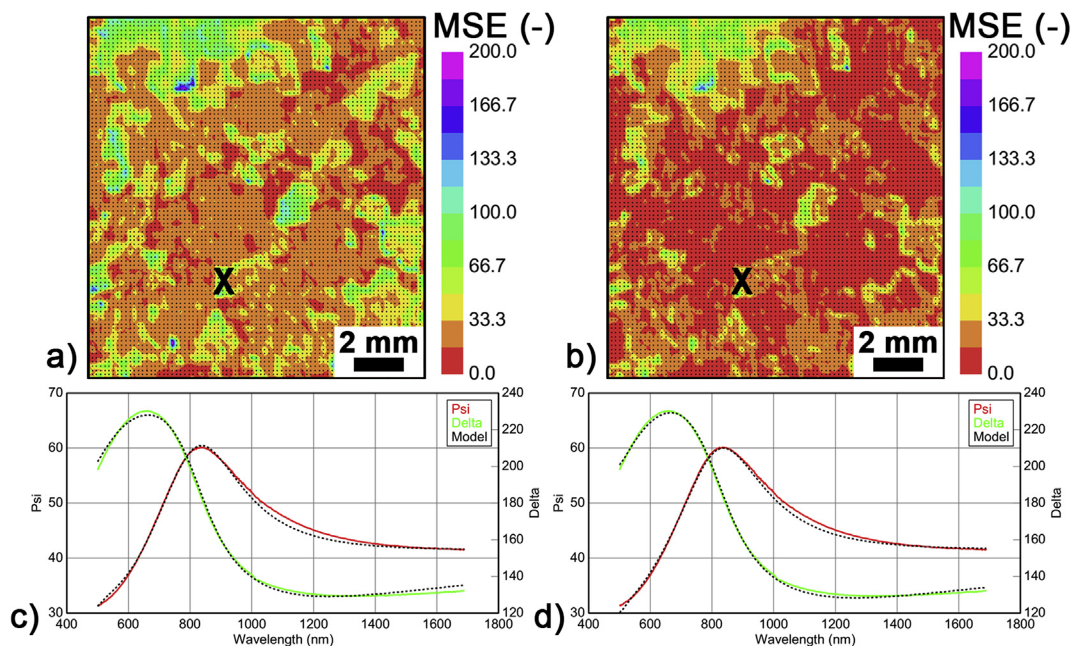

Fig. 5 – Mean square error of fitting using a constant (a, c) and an exponentially decaying (b, d) Cauchy dispersion *A* parameter in the function of depth within the layer, over the entire surface (a, b) and at the marked points (d, e).

3.2. XPS and chemical composition

Since the grain size shown by optical microscopy is smaller than the detectable area of XPS, the measured compositions are an average over several grains. The composition was determined at the surface that received only small ion sputtering to reduce the carbon contamination and at some larger depths along the layer thickness. The calculated concentration values of atomic% are shown in Table 3.

Since the binding energies of carbon with different chemical bonds are different, the surface contamination consisting of mainly simple organic carbon chains (284.6eV) can be separated from CO_3 (~289 eV), which is a real component of the layer. Thus, the table contains only the contribution from CO_3 type carbon signal, which is decreasing with the increasing depth. It is important to note that the organic contamination may also contain some carboxyl state (-O-C=O) carbon atoms whose binding energy coincides with the inorganic CO_3. Therefore, the calculated CO_3 value may be somewhat overrated at the surface (marked as 1 nm in the table). The measured oxygen content is probably exceeding the real one because the surface contamination has some oxygen

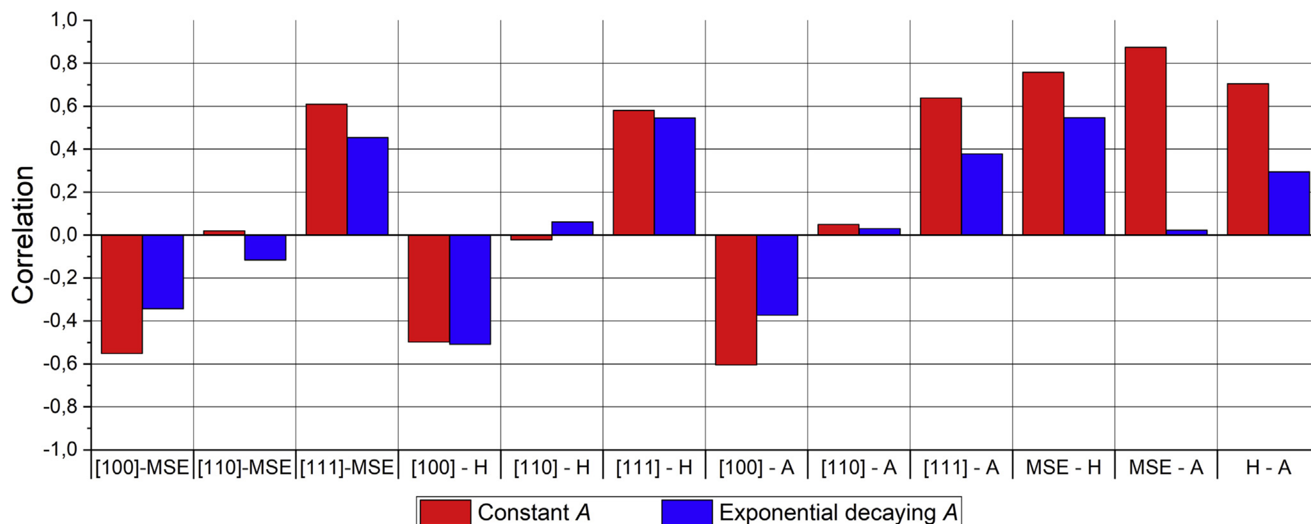

Fig. 6 – Correlation coefficients between the main crystallographic orientations ([100], [110], and [111]), the mean square error of fitting (MSE), the measured layer thickness (*d*), and parameter *A*, which determine the refractive index. The maximum of parameter *A* was used in the exponentially decaying case, which is at the layer–substrate interface.

Table 3 – Detected elements with XPS in two different depths in atomic%.

Depth	Fe	N	O	C	S
1 nm	19.0	1.5	68.2	7.5	3.8
20 nm	31.7	0.7	61.5	1.6	4.5
40 nm	29.7	0.9	63.5	1.3	4.6
60 nm	54.1	0.7	40.7	1.3	3.3
80 nm	70.5	0.4	27.0	0.7	1.4

contribution too to the detected oxygen peak. Consequently, the calculated oxygen concentration involved a slight correction for this.

Besides atomic concentrations, the chemical state of components was also revealed by XPS measurements. As expected, the topmost nanometers of the layer were oxidized due to air exposure. A Fe peak could be identified as a near stoichiometric Fe_2O_3 compound in the observed range (~5–6 nm). The S peak showed a mixture of SO_4 and S_2O_3 states with SO_4 dominance. Because the S peak's kinetic energy is double that of the Fe peak, the statements of S compounds concern ~8–10 nm. However, it allows a somewhat free interpretation regarding their location in this range, supposing either a homogeneous SO_4 and S_2O_3 distribution or more SO_4 at the top and less at the depth. Reaching larger depth, Fe showed a mixture of different states Fe^{3+} - Fe^{2+} - Fe. Finally, the metallic Fe state becomes dominant at the bottom of the layer. The development of the Fe-related peaks in the function of depth is shown in Fig. 7b.

The binding energy of detected sulfur atoms showed that sulfur is in a more or less oxidized form in the layer. Two chemical states can be distinguished: one is a fully oxidized state of SO_4, and one is a partially reduced state of S_2O_3. The oxidation states changed with depth in accordance with the expectations that the sulfur at the surface is more oxidized, exhibiting a mixture of S_2O_3 and SO_4 states, while in the 20 nm depth, it is dominantly in the S_2O_3 state (as shown in Fig. 7a). Below the top few nanometers, the chemical states of sulfur were more or less stable, keeping a 20% SO_4 and 80% S_2O_3 ratio down to the bottom of the layer. Determination of this ratio involves a higher error rate because sulfur is a minor component of ~4%.

3.3. *Discussion - proposed model*

During color etching the Fe atoms are dissolved from the ferrite grains and form different compounds over the grain, that compose an interfering layer. It was shown previously that a thicker layer after a given time of etching corresponds to faster Fe dissolution [17,21]. The formation of Fe compounds requires the appropriate anions from the solution that – after an initial layer is formed – have to diffuse through the forming layer. This may create a diffusion limitation that affects the kinetics of layer formation and may lead to a Fe-rich region close to the ferrite–layer interface and a Fe-poor region at the top of the layer. The differences in the Fe content and the composition of Fe compounds (transition from sulfate to metabisulfite, decreasing oxygen content) are confirmed by XPS measurements performed in increasing depths. This explains why the exponentially decaying RI model fits the ellipsometry data better. Since Fe and Fe-rich compounds have a higher RI, the RI would decay from the ferrite–layer interface hand-in-hand with the Fe content.

Figure 8 presents the previous and the modified, proposed model to interpret the RI of the interfering layer upon color etching. The previous model presumed that the RI is the same for all grains and also that the layer is homogeneous along its thickness (Fig. 8a). This way, the resulting color difference after etching for a given amount of time was only the effect of different layer thickness, originating from different etching speeds and ultimately the different corrosion resistance for the individual grains. The smaller the closed angle between the orientation of a particle and the direction [100], the faster the etching process is.

However, in Fig. 4.a, it could be seen that the RI of the layer varies between the grains. Besides, optimized modeling of the obtained ellipsometry data proved that the RI of the layer is not homogeneous along its thickness but decays exponentially from the ferrite–layer interface, as depicted in Fig. 8.b. XPS data also confirmed that the decay of RI can be associated with the varying chemical composition and Fe content.

The differences in grain etching speeds in the function of grain orientation and the weak correlation between A and the main angles (see Fig. 6) also suggest that the

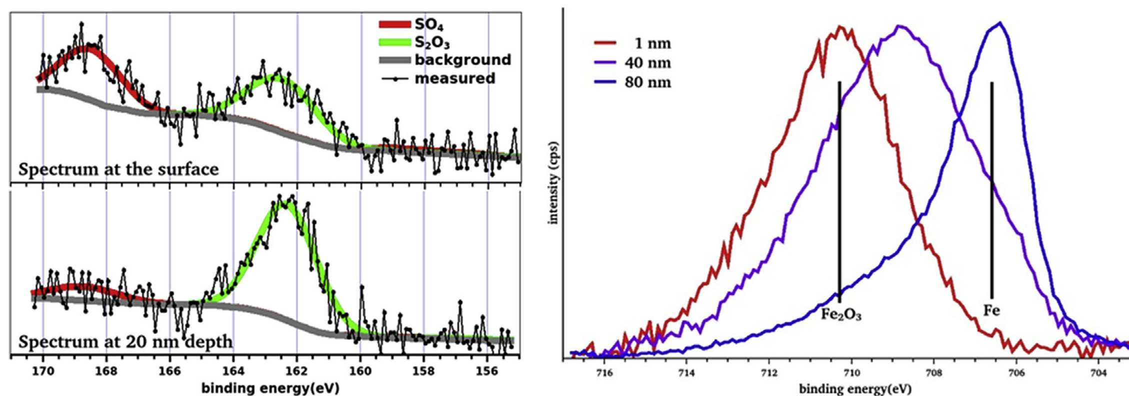

Fig. 7 – a) XPS spectra corresponding to sulfur-related peaks detected in two depths on the surface of the sample. b) Normalized Fe 2p 3/2 peak measured at different depths. Nominal positions of the peaks in metallic Fe and in Fe_2O_3 are presented by black lines.

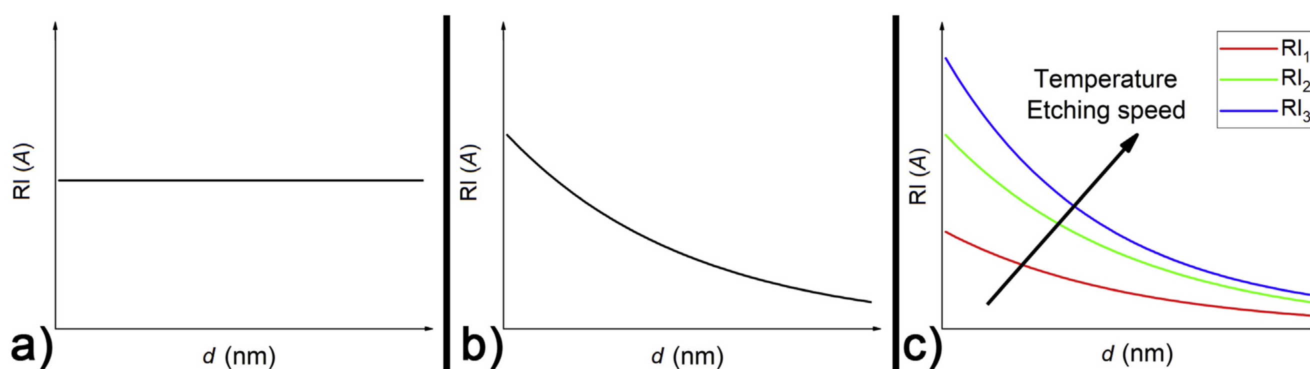

Fig. 8 – Illustrations of the refractive index as a function of position within the layer. Constant RI for the whole layer (a), exponential decaying RI, which is the same for all grains (b) and exponential decaying RI for different grain orientations (c).

individual ferrite grains have different $n(A)$ vs. d characteristics (Fig. 8c), depending on their orientation. If the resulting refractive index of the developed film would only depend on the etching time (and the $n(A)$ vs. d curve would be the same for all grains, as in Fig. 8b), then parameter A (and RI) would not change among the grains. Besides, there would be a strong negative correlation between A and d, indicating a lower RI for thicker layers. The positive correlation between A and d, which drops to a weak 0.3 for the exponentially decaying model, proves that the different grains cannot have the same $n(A)$ vs. d curves. The presented results prove that faster layer build-up goes hand in hand with faster Fe dissolution, leading to inhomogeneous chemical composition and RI along the thickness of the interfering layer.

4. Conclusions

The structural and chemical homogeneity of the interfering layer, that was developed during color etching a low-carbon steel specimen with Beraha-I type color etchant was investigated. It was shown that: 1) the refractive index of the layer above the individual grains is varying depending on the crystallographic orientation of the grains in the same way as the etching speed/developed layer thickness does; 2) the RI of the layer is not constant, it has a maximum at the ferrite–layer interface and decays towards the top of the layer; 3) the differences in the obtained RI along the layer thickness correlates well with the measured chemical composition with XPS (decreasing Fe content from the interface and increasing O content in the same time). The presented results greatly help in the refinement of models that are used to correlate the color of color etching with the crystallographic orientation of the grains.

Data availability

The data presented in this study are available on request from the corresponding author.

Declaration of Competing Interest

The authors declare that they have no known competing financial interests or personal relationships that could have appeared to influence the work reported in this paper.

Acknowledgment

Supported by the ÚNKP-21-3-II-259 New National Excellence Program of the Ministry for Innovation and Technology from the source of the National Research, Development and Innovation Found. Fund as well as by the Hungarian National Science Fund OTKA (Grant No. K131515). This research was funded by the National Research, Development, andInnovation Fund of Hungary under Grant TKP2021-EGA-02.

REFERENCES

[1] Petzow G. Metallographic etching. In: Techniques for metallography, ceramography, plastography. 2nd ed. ASM International; 1999. p. 1–240. ISBN 1615032207, 9781615032204.
[2] Beraha E. Ätzmittel zur Sichtbarmachung chemischer und physikalischer Inhomogenitäten in Stahlgefügen. Prakt Metallogr 1967;4(8):419–20.
[3] Webel J, Gola J, Britz D, Mücklich F. A new analysis approach based on Haralick texture features for the characterization of microstructure on the example of low-alloy steels. Mater Char 2018;144:584–96.
[4] Radzikowska JM. Effect of specimen preparation on evaluation of cast iron microstructures. Mater Char 2005;54(4–5):287–304.
[5] San Martin GD, Rivera Diaz del Castillo PEJ, Peekstok E, van der Zwaag S. A new etching route for revealing the austenite grain boundaries in an 11.4% Cr precipitation hardening semi-austenitic stainless steel. Mater Char 2007;58(5):455–60.
[6] Um HD, Kim N, Lee K, Hwang I, Seo JH, Yu YJ, et al. Versatile control of metal-assisted chemical etching for vertical silicon microwire arrays and their photovoltaic applications. Sci Rep 2015;5:11277.

[7] Durmaz AR, Müller M, Lei B, Thomas A, Britz D, Holm EA, et al. A deep learning approach for complex microstructure inference. Nat Commun 2021;12:6272.
[8] Heimann RB. Principles of chemical etching — the art and science of etching crystals. In: Grabmaier J, editor. Silicon chemical etching. Crystals (growth, properties, and applications). vol. 8. Berlin, Heidelberg: Springer; 1982. p. 175–221.
[9] García L, Dietz C, Criado A, Martínez JA. Colour metallography of cast aluminium alloys. Pract Metallogr 2014;51:514–29.
[10] Vaško A, Belan J, Tillová E. Use of colour etching in the structural analysis of graphitic cast irons. Manufacturing Technology 2020;20(6):845–8.
[11] Schaberger E, Grote F, Schievenbusch A. Colour etching and coloured image analysis - a way of characterising the microstructures of innovative cast materials. Pract Metallogr 2000;37:419–34.
[12] Beraha E. Farbätzung für Gußeisen, Stähle, Werkzeugstähle, Manganstähle und ferritische und martensitische rostfreie Stähle. Prakt Metallogr 1971;8(9):547–50.
[13] Vander Voort G. Metallography, principles and practice. New York: McGraw-Hill Book Co.; 1984. ASM International, Materials Park, Ohio.
[14] Tillová E, Kuchariková L, Chalupová M, Belan J, Vaško A, Herčko A. Advantages of colour etching in quality control of recycled Al-Si cast alloys. Quality Production Improvement-QPI 2019;1:296–303.
[15] Vander Voort GF. Color metallography. In: ASM handbook. vol. 9. Metallography and Microstructures; 2004. p. 493–512.
[16] Renkó JB, Bonyár A, Szabó PJ. Effect of Beracha-I type color etchant on the ferrite phase in different type Fe-C alloys. In: IOP conference series: materials science and engineering. vol. 903; 2020. p. 12054. https://doi.org/10.1088/1757-899X/903/1/012054.
[17] Bonyár A, Renkó JB, Kovács D, Szabó PJ. Understanding the mechanism of Beraha-I type color etching: determination of the orientation dependent etch rate, layer refractive index and a method for quantifying the angle between surface normal and the ⟨100⟩, ⟨111⟩ directions for individual grains. Mater Char 2019;156:109844.
[18] Szabó PJ, Kardos I. Correlation between grain orientation and the shade of color etching. Mater Char 2010;61(8):814–7.
[19] Müller M, Britz D, Mücklich F. Scale-bridging microstructural analysis – a correlative approach to microstructure quantification combining microscopic images and EBSD data. Pract Metallogr 2021;58:408–26.
[20] Kardos I, Gácsi Z, Szabó PJ. Color etching for characterization the grain orientati-on in spheroidal graphite cast iron. Mater Sci Forum 2007;389:537–8.
[21] Bonyár A, Szabó PJ. Correlation between the grain orientation dependence of color etching and chemical etching. Microsc Microanal 2012;18(6):1389–92.
[22] Britz D. Opening the door to fundamental understanding of structure and color metallography - a correlative microscopy study on steel. Microsc Microanal 2014;834.
[23] Britz D. Reproducible surface contrasting and orientation correlation of low-carbon steels by time-resolved Beraha color etching. Mater. Perform. Characterization 2016;5(5):553–63.
[24] Britz D, Steimer Y, Mücklich F. New ways in metallography: through controlled conditions to objective microstructure analysis of low-carbon steels by LePera-etching, 100 Years of E04 development of metallography standards. 2019. p. 130–51.
[25] Bioud YA, Boucherif A, Belarouci A, Paradis E, Drouin D, Arès R. Chemical composition of nanoporous layer formed by electrochemical etching of p-type GaAs. Nanoscale Res Lett 2016;11:446.
[26] Aspnes DE. Spectroscopic ellipsometry—a perspective. J Vac Sci Technol: Vacuum, Surfaces, and Films 2013;31(5):058502.
[27] Vedam K. Spectroscopic ellipsometry: a historical overview. Thin Solid Films 1998;313–314:1–9.
[28] Houska J, Blazek J, Rezek J, Proksova S. Thin Solid Films 2012;520:5405–8.
[29] Lohner T, Serényi M, Petrik P. Characterization of sputtered aluminum oxide films using spectroscopic ellipsometry. Int. J. of New Horizons in Phys. 2015;2(1):1–4.
[30] Gooch JW. Encyclopedic dictionary of polymers. New York: Springer; 2007.
[31] Vincent Crist B. Handbook of monochromatic XPS spectra. Wiley; 2000.